Photoacoustic microscopy image resolution enhancement via directional total variation regularization

Zhenghua Wu (伍政华)[1], Mingjian Sun (孙明健)[1*], Qiang Wang (王 强)[1], Ting Liu (刘 婷)[1], Naizhang Feng (冯乃章)[1], Jie Liu (刘 劼)[1,2], and Yi Shen (沈 毅)[1]

[1]*Department of Control Science and Engineering, Harbin Institute of Technology, Harbin 150001, China*

[2]*Microsoft Research, Redmond 98052, USA*

[*]*Corresponding author: sunmingjian@hit.edu.cn*

Received August 16, 2014; accepted October 24, 2014; posted online November 28, 2014

Photoacoustic microscopy (PAM) is recognized as a powerful tool for various microcirculation system studies. To improve the spatial resolution for the PAM images, the requirements of the system will always be increased correspondingly. Without additional cost of the system, we address the problem of improving the resolution of PAM images by integrating a deconvolution model with a directional total variation regularization. Additionally, we present a primal-dual-based algorithm to solve the associated optimization problem efficiently. Results from both test images and some PAM images studies validate the effectiveness of the proposed method in enhancing the spatial resolution. We expect the proposed technique to be an alternative resolution enhancement tool for some important biomedical applications.

OCIS codes: 100.3020, 170.5120, 330.6130.

doi: 10.3788/COL201412.121701.

Photoacoustic microscopy (PAM) has been recognized as a vital tool for many biomedical studies and research applications due to the capability of high-resolution deep tissue imaging[1–7]. Up to now, PAM is always implemented by scanning the field-of-view on a point-by-point basis. In PAM system, to enhance the lateral resolution for optical-resolution PAM (OR-PAM), the optical numerical aperture (NA) should be increased[8,9]. At the same time, the corresponding working distance and thus the penetration depth will also be decreased[10]. Besides, in the experiments the optical scanning devices should have higher performance indexes, which imply more hardware requirements of the system. For another form of PAM, acoustic-resolution PAM(AR-PAM), the spatial resolution is based on the AR of the transducer[11]. To improve the resolution, higher performance ultrasound transducer need to be provided.

Many efforts have been made to improve the spatial resolution without increasing cost of the system, resulting in some advanced data acquisition schemes and novel signal processing methods[10,12,13]. Very different from these state-of-art technologies, we want to improve the spatial resolution directly from the low-resolution PAM images in this letter. To reconstruct a high-resolution image from one or more of the low-resolution observations is sometimes called super-resolution technology. Significant efforts have been made to address this problem. Yang *et al.* proposed to use sparsity as prior knowledge for patch-based image super-resolution[14]. A feedback-control framework without the information learned from other examples was proposed by Shan *et al.*[15]. Candes *et al.* presented a framework to super-resolve planar regions taken from 3D scenes via transform-invariant group-sparse regularization[16]. It is worth noting that this technology has been successfully applied to magnetic resonance imaging as an off-line image processing tool to increase the spatial resolution[17,18].

In general, we cannot recover the absent details from the low-resolution image, but we expect to hallucinate some specific textures that are visually pleasing[16]. Therefore, it is very important to exploit the potential information in the observed low-resolution images as prior knowledge. In this letter, we explore the use of directional total variation (DTV) to spatial resolution enhancement for PAM images. PAM images with some orientational structures are very common, such as information of vessel diameter, hemoglobin oxygen saturation, blood flow velocity, and other cellular microstructures. Specifically, we propose a formulation that integrates a deconvolution model with this sparsity promoting penalty. Additionally, an efficient alternate iteration scheme is also presented to solve the associated optimization problem. Finally, the proposed resolution enhancement approach has been validated by the studies of test image, thin bar copper, and 3D gelatin + graphite PAM images.

The spatial resolution enhancement problem we consider in this letter is how to recover a high-resolution image $S_H \in \mathbb{R}^{M\times N}$ from a given low-resolution image $S_L \in \mathbb{R}^{m\times n}$ $(M>m, N>n)$. The process from S_H to S_L can be modeled as a blurring combined with a downsampling process, that is

$$S_L = \mathscr{D}(K \otimes S_H), \tag{1}$$

 © 2014 Chinese Optics Letters

where K is a blurring kernel often considered as a Gaussian kernel, $\mathscr{D}$ denotes a downsampling operator: $\mathbb{R}^{M\times N}\rightarrow\mathbb{R}^{m\times n}$, and $\otimes$ is convolution operation. We can easily obtain another form of Eq. (1) by applying Plancherel's theorem, that is

$$\mathrm{S_L} = \mathscr{D}\mathscr{F}^{H}(\mathscr{F}(\mathrm{K})\mathscr{F}(\mathrm{S_H})), \tag{2}$$

where $\mathscr{F}$ and $\mathscr{F}^{H}$ are Fourier transform and inverse Fourier transform operators, respectively. To obtain the high-resolution image directly from unsampling the low-resolution image and then deconvolving it is extremely ill-posed. In this letter, we propose to use DTV[19] as non-quadratic regularization to incorporate stronger prior information into the reconstruction process.

Total variation (TV) is widely used as sparsity promoting penalty because of the advantages in terms of edge preservation and noise removal. But it often fails to improve the resolution of images with a few dominant directions. DTV has been presented to adapt high-level structures of the images and increase sensitivity at some certain directions. TV of an image $\mathrm{S_H}(i, j)$ can be expressed as

$$\mathrm{TV}(\mathrm{S_H})=\sum_{i,j}\sup_{\mathrm{v}(i,j)\in B_2}\langle\nabla\mathrm{S_H}(i,j),\mathrm{v}(i,j)\rangle, \tag{3}$$

where B_2 is the unit ball with l_2 norm, $\mathrm{v}(i, j)$ is a vector with the same dimension as $\nabla\mathrm{S_H}(i, j)$, $\nabla\mathrm{S_H}(i, j) = (\nabla^1\mathrm{S_H}(i, j); \nabla^2\mathrm{S_H}(i, j))$, ∇^1 and ∇^2 are horizontal and vertical difference operators, respectively. DTV is realized by replacing B_2 with an ellipse $E_{\alpha,\theta}$ with an oriented angle θ and a major axis of length $\alpha > 1$. Thus, the definition of DTV[19] can be written as

$$\mathrm{DTV}(\mathrm{S_H})=\sum_{i,j}\sup_{\mathrm{v}(i,j)\in E_{\alpha,\theta}}\langle\nabla\mathrm{S_H}(i,j),\mathrm{v}(i,j)\rangle. \tag{4}$$

Moreover, the relationship between $E_{\alpha,\theta}$ and B_2 can be expressed as $E_{\alpha,\theta} = R_\theta T_\alpha B_2$, where

$$R_\theta = \begin{pmatrix}\cos\theta & -\sin\theta\\ \sin\theta & \cos\theta\end{pmatrix}, T_\alpha = \begin{pmatrix}\alpha & 0\\ 0 & 1\end{pmatrix}. \tag{5}$$

If we use R_θ, T_α to represent the corresponding operators that act on the vector fields, Eq. (4) can be rewritten as

$$\mathrm{DTV}(\mathrm{S_H}) = \sup_{\mathrm{v}(i,j)\in R_\theta T_\alpha B_2}\langle\nabla\mathrm{S_H},\mathrm{v}\rangle = \sup_{\mathrm{v}(i,j)\in B_2}\langle\nabla\mathrm{S_H},R_\theta T_\alpha\mathrm{v}\rangle. \tag{6}$$

Given the model in Eq. (2) and the DTV regularization term, we propose to reconstruct $\mathrm{S_H}$ from $\mathrm{S_L}$ by using

$$\hat{\mathrm{S}}_\mathrm{H} = \underset{\mathrm{S_H}}{\mathrm{argmin}}\frac{1}{2\lambda}\left\|\mathscr{D}\mathscr{F}^{H}(\mathscr{F}(\mathrm{K})\mathscr{F}(\mathrm{S_H}))-\mathrm{S_L}\right\|_2^2+\mathrm{DTV}(\mathrm{S_H}), \tag{7}$$

where λ is a regularization parameter.

We propose to use a primal-dual-based algorithm to solve Eq. (7) with DTV penalty. Firstly, Eq. (7) can be reformulated as the following convex–concave saddle-point problem:

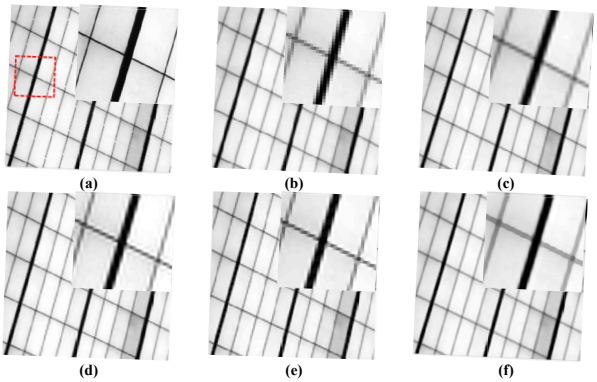

Fig. 1. Results from a test image with the upsampling factor of 4: (a) original 512×512 image, (b) input 128×128 low-resolution image, (c) result of bicubic interpolation, (d) result of sparse coding[14], (e) result of TV reconstruction, and (f) result of DTV reconstruction.

where $V=\{\mathrm{v}\in\mathbb{R}^{2MN\times1}|\|\mathrm{v}\|\infty\le1\}$. With the fact that $\mathrm{R}_\theta{}^*=\mathrm{R}_{-\theta}$ and $\mathrm{T}_\alpha{}^*=\mathrm{T}_\alpha$ (A^* denotes the adjoint operator of A), and the adjoint operators of the above corresponding operators, we can solve Eq. (8) by the following alternate iteration scheme:

$$\mathrm{v}^{(k+1)} = Proj_V(\mathrm{v}^{(k)}+\delta\mathrm{T}_\alpha\mathrm{R}_{-\theta}\nabla\bar{\mathrm{S}}_\mathrm{H}^{(k)}), \tag{9}$$

$$\mathrm{r}^{(k+1)} = Prox_2^\delta(\mathrm{r}^{(k)}+\delta(\mathscr{D}\mathscr{F}^{\mathrm{H}}(\mathscr{F}(\mathrm{K})\mathscr{F}(\bar{\mathrm{S}}_\mathrm{H}^{(k)}))-\mathrm{S_L})), \tag{10}$$

$$\mathrm{S}_\mathrm{H}^{old} = \mathrm{S}_\mathrm{H}^{(k)}, \tag{11}$$

$$\mathrm{S}_\mathrm{H}^{(k+1)} = \mathrm{S}_\mathrm{H}^{(k)}+\tau(div_1(\mathrm{R}_\theta\mathrm{T}_\alpha\mathrm{v}^{(k+1)}) - \mathscr{F}^{-\mathrm{H}}(\mathscr{F}(\mathrm{K})^{\mathrm{H}}\mathscr{F}(\mathscr{D}*(\mathrm{r}^{(k+1)})))), \tag{12}$$

$$\bar{\mathrm{S}}_\mathrm{H}^{(k+1)} = 2\mathrm{S}_\mathrm{H}^{(k+1)}-\mathrm{S}_\mathrm{H}^{old}, \tag{13}$$

where $Proj_V(\bar{\mathrm{v}}) = \mathrm{v}/(\max(1, |\bar{\mathrm{v}}|))$ is the Euclidean projector, $Prox_2^\delta(\bar{r}) = \bar{r}/(1+\delta\lambda)$ is the proximal map, and $(div_1)^* = -\nabla$ (refer to Ref. [20] for further details). We followed the instructions given in Refs. [20, 21] and chose the step-sizes $\delta = \tau = 1/\sqrt{12}$ to guarantee the convergence. Furthermore, the initial values of the variables were set to be 0 in this letter.

A carefully selected test image (Fig. 1(a)) has been provided to evaluate the performance of our proposed method. This experimental result is presented because the test image has the corresponding high-resolution reference image and a dominant direction, which allows quantitative analysis. The oriented angle θ was determined by minimizing the values of DTV as θ varies (as in Ref. [19]). Figure 2 shows the changes of the DTV values of Fig. 1(a) while the oriented angle varies, as can be seen, the minimum value is obtained at $\theta = -\pi/12$, which is chosen as the parameter for our study, and we chose $\alpha = 3$ in this simulation experiment.

$$\left\{\hat{\mathrm{S}}_\mathrm{H},\hat{\mathrm{v}},\hat{\mathrm{r}}\right\} = \underset{\mathrm{S_H}}{\mathrm{argmin}}\max_{\mathrm{v}\in V,\mathrm{r}}\left\langle\nabla\mathrm{S_H},\mathrm{R}_\theta\mathrm{T}_\alpha\mathrm{v}\right\rangle+\left\langle\mathscr{D}\mathscr{F}^{-\mathrm{H}}(\mathscr{F}(\mathrm{K})\mathscr{F}(\mathrm{S_H}))-\mathrm{S_L},\mathrm{r}\right\rangle-\frac{\lambda}{2}\left\|\mathrm{r}\right\|_2^2, \tag{8}$$

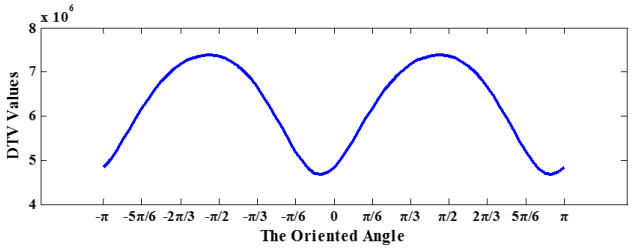

Fig. 2. Curve of the DTV values of the image shown in Fig. 1(a) while the oriented angle 6 varies.

We applied a magnification factor of 4 for this test image, and the blurring kernel in Eq. (1) was chosen as a 13×13 Gaussian kernel with standard deviation dependent on the magnification factor (we used 1.8 for a factor of 4, which was followed by the instructions in Ref. [16]). The Matlab function *imresize* was also used to realize the bicubic interpolation, which can be modeled as the downsampling operator $\mathscr{D}$ and upsampling operator $\mathscr{D}^*$.

Figures 1(c)–(f) show a set of representative experimental results from the study described above. As can be seen, the result from bicubic interpolation is very blurry, the sparse coding result is slightly better but still cannot preserve the edges very well. Result from TV regularization is with significant jagged artifacts, which leads to wobbly edges. The reconstruction based on DTV regularization provides high spatial resolution and superior quality in edge preservation, that is, clear straight edges. To better illustrate the performance, we evaluate the results quantitatively in root-mean-square errors (RMSEs) defined as $\sqrt{\sum_{i=1}^{M}\sum_{j=1}^{N}(S_{ij}-\hat{S}_{ij})^2/MN}$ where S is the reference image and $\hat{S}$ denotes the estimated image. The RMSEs for Figs. 1(c)–(f) are 12.2137, 11.9951, 12.4813, and 11.4126, respectively, which agree with the qualitative comparison. It is also worth noting that although the proposed method provides small improvement in RMSE, it has the exciting visual effects.

Some PAM images have also been used to validate the effectiveness of the proposed method. In this letter, a combined laser-scanning OR-PAM with optical microscope system has been set up in transmission mode. In the system, the excitation part is a diode-pumped Nd:YLF Q-switched pulsed laser (wavelength 523 nm, duration time 6 ns; IS8II-E, INNOSLAB Edgewave, Germany). The maximum pulse repetition rate of the laser is up to 5 kHz. The laser beam is focused into the object by an air-conditioned optical objective and optically scanned by the 2D precision motor (Z-108, Thorlabs, Newton, USA) to form optical and photoacoustic images, which image the dual contrasts of optical absorption and optical intensity simultaneously.

In our first experiment, the sample is Agar/UK G2730C 400 mesh thin bar copper with 8 μm linewidth and 52 μm interval. The optical objective is Qiset Microscope Objective (magnification: 10×, NA: 0.25, focal length: 15.8 mm, objective length: 34.0 mm). Furthermore, the image area, step size, x y steps, and average times are 300×300 (μm), 3 μm, 100×100, and 10, respectively. And the photoacoustic signals generated from the sample are received by the 20 MHz focused ultrasound transducer. Figure 3(a) shows the PAM result from such setups. For the high-resolution reconstruction, the parameters for DTV-based algorithm are the same with the test image study except θ, we chose $\theta=-\pi/3$ in this letter. Furthermore, it is worth mentioning here that the parameters for DTV (namely (α, θ)) should be chosen carefully. If the dominant angle is reliable or distinct, an appropriate higher value of α may guarantee better performance, otherwise, a smaller α is suggested. Please refer to Ref. [19] for further discussion about the effect of (α, θ) parameters in terms of the reconstruction performance. Figures 3(b)–(d) show the high-resolution results from different methods. As can be seen, the sparse coding and TV reconstruction both have over-smoothing problems, whereas the DTV reconstruction provides clearer edges and holds more details compared with the other two methods. Alternatively, we use entropy and mean gradient of a single image for the quantitative analysis in this letter since there is no reference high-resolution image. The widely used image entropy and mean gradient can describe the amount of information and the detail variation of an image, respectively. The values of entropy and mean gradient in Fig. 3 are shown in Table 1, we can see that the DTV result holds the largest values, which may imply that it has the most information and texture features.

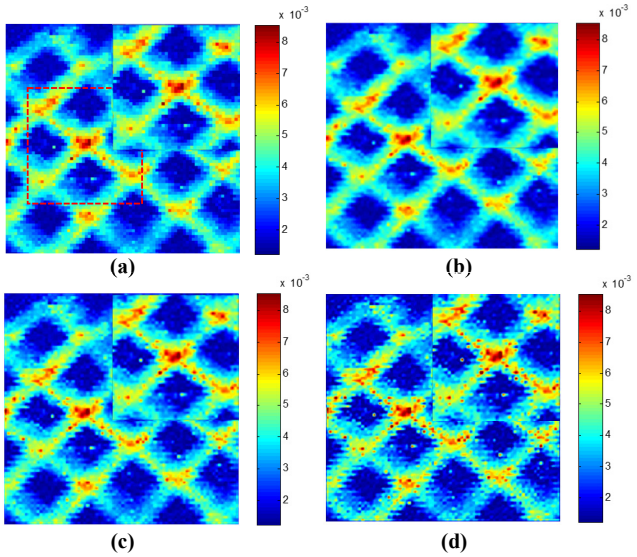

Fig. 3. Results from enhancing resolution of thin bar copper image with the upsampling factor of 4: (a) low-resolution 100×100 PAM image, (b) 400×400 result of sparse coding, (c) 400×400 result of TV reconstruction, and (d) 400×400 result of DTV reconstruction.

Table 1. Values of Image Entropy and Mean Gradient in Fig. 3

Type of Values	Fig. 3(a)	Fig. 3(b)	Fig. 3(c)	Fig. 3(d)
Image Entropy	0.9630	0.9756	0.9897	1.0556
Mean Gradient	4.5×10^{-5}	6.7×10^{-5}	1×10^{-4}	7.4×10^{-4}

Table 2. Values of Image Entropy and Mean Gradient in Fig. 4

Type of Values	Fig. 4(a)	Fig. 4(b)	Fig. 4(c)	Fig. 4(d)
Image Entropy	1.0343	1.0364	1.0399	1.1302
Mean Gradient	3.5×10^{-5}	5.2×10^{-5}	8.6×10^{-5}	5.7×10^{-5}

In PAM experiments, the strongest photoacoustic signal generates where the phantom absorption density is greatest, the distribution of the phantom observed optically closely maps to the photoacoustic images. In our second experiment, the sample is 3D polyacrylamide gel (8% acrylamide + 0.5% bis-acrylamide) with graphite powder in a standard cell culture dish (PN: 16235-1SGP, 35×12 (mm), diameter: 20 mm), the optical objective is Nikon PH3 DL (plan magnification: 40×, NA: 0.65, working distance: 0.48 mm, tube length: 160). The sample includes many spots (different graphite granule distributions) in different layers. One spot of non-uniform distribution was selected for the optical scanning. The parameters for the image area, step size, x y steps, average times, and center frequency of focused ultrasound transducer are set to be 1.2×1.2 (mm), 10 μm, 120×120, 10, and 40 MHz, respectively. The value of 9 is $-5\pi/12$ in this letter. Figure 4 shows the PAM result and a set of representative high-resolution results. Figure 5 shows the close-ups of Fig. 4 identified by the red rectangles. Again, the relative entropy and mean gradient values are presented in Table 2. As expected, the DTV reconstruction holds the best performance of enhancing the spatial resolution for the PAM images, from both visual effects and quantitative analysis. Moreover, the DTV result can express more accurate details of the absorption of graphite powder distribution to microlevel.

In conclusion, we present a novel method for reconstructing high-resolution PAM images from low-resolution ones without increasing cost of the PAM system. An efficient primal-dual-based algorithm is described to solve the resulting optimization problem. We use both test image and some PAM images to demonstrate the improvement in enhancing the spatial resolution by the proposed method. Specifically, one can observe significantly clearer edges and details from the proposed high-resolution images. As we have made clear throughout this letter, the DTV-based method is geared to the images with some orientational edges or textures, otherwise, there can be some artifacts produced. In addition, since we do not incorporate any other prior information except the DTV, input images missing a mass of textures cannot be recovered. An important but also a difficult issue in the proposed technology is how to accurately estimate the blurring kernel rather than empirical selection, which is also our future research direction. Although the proposed technology sometimes can provide a little more thick edges and hallucinate the textures compared with the real high-resolution images, it is indeed effective in improving the spatial resolution. And we expect the proposed method to be an alternative tool to enhance the PAM images resolution.

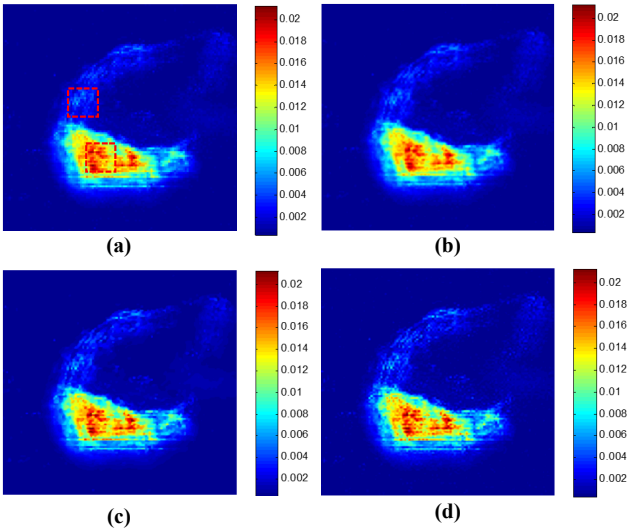

Fig. 4. Results from enhancing resolution of 3D gelatin + graphite image with the upsampling factor of 4: (a) low-resolution 120×120 PAM image, (b) 480×480 result of sparse coding, (c) 480×480 result of TV reconstruction, and (d) 480×480 result of DTV reconstruction.

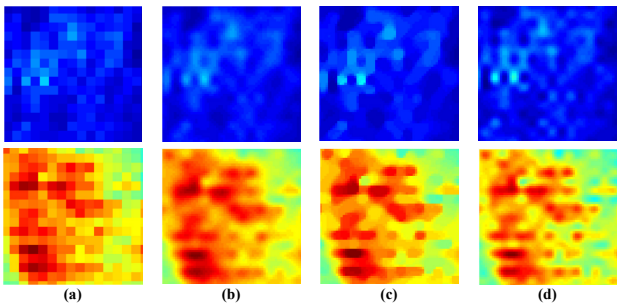

Fig. 5. Close-ups of Fig. 4 corresponding to the red rectangles: (a) close-ups of Fig. 4(a), (b) close-ups of Fig. 4(b), (c) close-ups of Fig. 4(c), and (d) close-ups of Fig. 4(d). As can be seen, the proposed result can show more accurate details of the absorption of graphite powder distribution to microlevel.

This work was supported by the National Natural Science Foundation of China (Nos. 61174016, 61201307, and 61371045) and the Fundamental Research Funds for the Central Universities (No. 2013132). The authors thank Prof. Paichi Li and the Ultrasound Imaging Laboratory of National Taiwan University, China, for the support.

References

1. H. F. Zhang, K. Maslov, G. Stoica, and L. V. Wang, Nat. Biotechnol. **24,** 848 (2006).
2. L. V. Wang, Nat. Photon. **3,** 503 (2009).
3. M. L. Li, H. F. Zhang, K. Maslov, G. Stoica, and L. V. Wang, Opt. Lett. **31,** 474 (2006).
4. C. Kim, S. Park, J. Kim, S. Lee, M. Jeon, J. Kim, and K. Oh, J. Biomed. Opt. **18,** 10501 (2013).
5. J. J. Yao and L. V. Wang, Laser Photon. Rev. **7,** 758 (2013).
6. X. Yang, X. Cai, K. Maslov, L. V. Wang, and Q. Luo, Chin. Opt. Lett. **8,** 609 (2010).
7. S. Ye, J. Yang, J. Xi, Q. Ren, and C. Li, Chin. Opt. Lett. **10,** 121701 (2012).
8. X. Chen, Y. Lei, Y. Wang, and D. Yu, Chin. Opt. Lett. **9,** 121001 (2011).
9. C. Zhang, K. Maslov, S. Hu, R. Chen, Q. Zhou, K. K. Shung, and L. V. Wang, J. Biomed. Opt. **17,** 020501 (2012).
10. J. H. Chen, R. Q. Lin, H. N. Wang, J. Meng, H. R. Zheng, and L. Song, Opt. Express **21,** 7316 (2013).
11. W. X. Xing, L. D. Wang, K. Maslov, and L. V. Wang, Opt. Lett. **38,** 52 (2013).
12. J. Meng, C. B. Liu, J. X. Zheng, R. Q. Lin, and L. Song, J. Biomed. Opt. **13,** 036003 (2014).
13. C. Zhang, K. Maslov, J. Yao, and L. V. Wang, J. Biomed. Opt. **17,** 116016 (2012).
14. J. C. Yang, J. Wright, T. S. Huang, and Y. Ma, IEEE Trans. Image Process. **19,** 2861 (2010).
15. Q. Shan, Z. R. Li, J. Y. Jia, and C. K. Tang, ACM Trans. Graph. **27,** 153 (2008).
16. C. F. Granda and E. J. Candes, in *Proceedings of 2013 IEEE International Conference on Computer Vision* 3336 (2013).
17. E. V. Reeth, I. W. K. Tham, C. H. Tan, and C. L. Poh, Concepts Magn. Reson. Part A **40,** 306 (2012).
18. S. H. Joshi, A. Marquina, S. J. Osher, I. Dinov, J. D. V. Horn, and A. W. Toga, in *Proceedings of 2009 IEEE International Symposium on Biomedical Imaging: From Nano to Macro* 161 (2009).
19. I. Bayram and M. E. Kamasak, IEEE Signal Process. Lett. **19,** 781 (2012).
20. A. Chambolle and T. Pock, J. Math. Imaging Vis. **40,** 120 (2011).
21. F. Knoll, K. Bredies, T. Pock, and R. Stollberger, Magn. Reson. Med. **65,** 480 (2011).